Polymer modelling unveils the roles of heterochromatin and nucleolar organizing regions in shaping 3D genome organization in *Arabidopsis thaliana*.

Marco Di Stefano[1*], Hans-Wilhelm Nützmann[2], Marc A. Marti-Renom[1,3,4,5], Daniel Jost[6*]

[1]*CNAG-CRG, The Barcelona Institute of Science and Technology (BIST), Barcelona, Spain*

[2]*The Milner Centre for Evolution, Department of Biology and Biochemistry, University of Bath, Bath, BA2 7AY, UK*

[3]*Universitat Pompeu Fabra, Barcelona, Spain*

[4]*CRG, The Barcelona Institute of Science and Technology (BIST), Barcelona, Spain*

[5]*ICREA, Barcelona, Spain*

[6]*Université de Lyon, ENS de Lyon, Univ Claude Bernard, CNRS, Laboratoire de Biologie et Modélisation de la Cellule, Lyon, France*

*corresponding authors: marco.distefano@cnag.crg.eu, daniel.jost@ens-lyon.fr

ABSTRACT

The 3D genome is characterized by a complex organization made of genomic and epigenomic layers with profound implications on gene regulation and cell function. However, the understanding of the fundamental mechanisms driving the crosstalk between nuclear architecture and (epi)genomic information is still lacking. The plant species *Arabidopsis thaliana* is a powerful model organism to address these questions due to its compact genome for which we have a rich collection of microscopy, Chromosome Conformation Capture (Hi-C), and ChIP-seq experiments. Using polymer modelling, we investigate the roles of nucleolus formation and epigenomics-driven interactions in shaping the 3D genome of *A. thaliana*. By validation of several predictions with published data, we demonstrate that self-attracting nucleolar organizing regions and repulsive constitutive heterochromatin are major mechanisms to regulate the organization of chromosomes. Simulations also suggest that interphase chromosomes maintain a partial structural memory of the V-shapes, typical of (sub)metacentric chromosomes in anaphase. Additionally, self-attraction between facultative heterochromatin regions facilitates the formation of Polycomb bodies hosting H3K27me3-enriched gene-clusters. Since nucleolus and heterochromatin are highly-conserved elements in eukaryotic cells, our findings pave the way for a comprehensive characterization of the generic principles that are likely to shape and regulate the 3D genome in many species.

INTRODUCTION

In eukaryotic cells, the genome structure is characterized by a complex three-dimensional (3D) organization (1–3) that plays a crucial role in regulating gene function and expression (4, 5), and in determining cell-fate decisions (6–9), and cell-development (6, 10).

Microscopy and chromosome conformation capture (3C) (11) techniques have been used to unveil the architectural folding of the genome. Using microscopy techniques such as FISH (12), 3D-FISH (13, 14) and cryo-FISH (15), it was possible to visualize that each chromosome occupies a distinct portion of the nucleus called chromosome territory (CT) with a non-random radial location (12–14). High-throughput chromosome conformation capture (Hi-C) (16) confirmed the presence of CTs by probing much stronger cis- than trans-chromosome interactions (16, 17). Analysis of Hi-C maps also revealed the presence of a typical checkerboard pattern that reflects the physical segregation of the genome into multi megabase chromatin compartments (16, 18). These are characterized by different GC-content, gene density and epigenomic marks, suggesting that they mostly match the classical partition of the genome in hetero- and euchromatin (19–22). At the sub-megabase level, Hi-C experiments also revealed that the genome is organized in self-interacting regions termed topologically associating domains (TADs) (17, 23, 24), that have been also visualized by super-resolution microscopy approaches (25). In mammals and *Drosophila melanogaster (D. melanogaster)*, TADs are considered the structural and functional units of the genome that define the regulatory landscape (26–28).

In animals, computational studies based on polymer modelling enabled to relate the organizational layers of the genome to specific active and passive physical mechanisms. The formation of chromosome territories may be facilitated by the slow relaxation dynamics of topologically-constrained polymers (29–32). The segregation between active and repressive chromatin compartments was suggested to be primed by micro-phase separation promoted by proteins such as heterochromatin protein 1 (HP1) and polycomb group (PcG) proteins binding to repressive histone marks (33–37). The formation of TADs was associated with mechanisms of active (38, 39) or passive (40) loop-extrusion.

Within plants, *Arabidopsis thaliana* (*A. thaliana*) is an important model organism for structural genomics studies and has the most comprehensive collection of chromosome data available. Its genome, that is constituted by 5 chromosomes, is diploid, and is smaller (~120 mega-base pairs, Mbp) and gene-denser compared to other plant genomes, which makes it more suitable for computational studies.

In interphase, *A. thaliana* chromosomes are organized as well-defined chromosome territories (41–45) with generally no preferential radial positioning nor chromosome pairing (41, 46, 47). Notable exceptions lie in the short arms of acrocentric chromosomes 2 and 4, that bear the nucleolus-organizing regions (NOR2 and NOR4) and typically associate in a single central nucleolus (41, 48–50). At the nucleolar periphery, the telomeres appear to be clustered (42–46). Within chromosome territories, *A. thaliana* chromatin contains active and repressive chromatin (51), that, differently from mammals and *D. melanogaster* (16, 17) in which they form large compartments of ~100 kbp, are organized in smaller domains (42, 43). The chromocenters (including centromeres and peri-centromeres), that are the largest heterochromatic regions, are spatially and dynamically confined at the nuclear periphery (41, 46, 52, 53) and anchor protruding euchromatic loops of about 0.1-1.5 mega-base pairs (Mbp) resulting in a looped *rosette* overarching structure (46). In individual nuclei, chromocenters may also self-associate, leading to trans-chromosome contacts and larger heterochromatin foci (42–46). Hi-C data have also revealed the existence of long-range cis- and trans-chromosomal contacts, the so-called KNOT Engaged Elements (a.k.a. IHIs) structure [42,43] that has structural counterparts in other plant species such as the compact silent centre (CSC) in rice (54). At fine scales, although TADs are not prominent features (44, 55), TAD-boundary-like elements have been shown to correlate with open chromatin and actively transcribed genes (44), and local self-interacting domains can be formed between H3K27me3-enriched gene-clusters (56). At the scale of a few kilo-base pairs (kbp), local chromatin loops are suggested to connect the 5' and 3' ends of genes (45).

Previous modelling exercise (57), using a phenomenological ad-hoc coarse-grained polymer model, have suggested that the peripheral positioning of the chromocenters and the central localization of the nucleoli may be the consequences

of entropic forces emerging from the formation of large permanent intra-chromosome loops and of steric constraints. However, a detailed description and characterization of the specific biological and Physico-chemical mechanisms leading to the genome organization in *A. thaliana* is still missing.

Here, we test the hypothesis that epigenomics, as previously suggested (44, 45, 51, 58, 59), is a driving force of the genome structural organization in *A. thaliana (60)*. We use polymer modelling and molecular dynamics together with epigenomic data to generate genome-wide chromosome models. By providing quantitative comparisons of our predictions with Hi-C and microscopy data, we demonstrate that three fundamental elements may be sufficient to determine the genome organization in *A. thaliana.* First, chromosomes need to be preconditioned as V-shaped objects. Second, the self-attraction of NORs shapes the overall nuclear organization. Third, the repulsion between constitutive heterochromatin and other epigenomic states explains the segregation and the localization at the nuclear periphery of chromocenters. At local scales, the self-attraction between facultative heterochromatin regions recovers the formation of self-interacting gene-clusters.

MATERIAL AND METHODS

Our work consists of three main parts: (1) processing of ChIP-seq datasets to classify the *Arabidopsis thaliana (A. thaliana)* chromosomes in epigenomic states; (2) genome-wide molecular dynamics simulations models, and (3) analysis of the obtained 3D models and validation against published experimental data.

Epigenomic states analyses.

ChIP-seq epigenomic data at 400 bp of resolution for 4 histone marks: H3K4me2, H3K4me3 (signatures of active genes), H3K27me3 (signature of facultative, polycomb-like heterochromatin), and H3K9me2 (specific to constitutive heterochromatin) were collected from previously published works (44, 45). To each 3kbp-genomic region of the genome, an average epigenomic signal was assigned for each of the 4 marks. A K-means algorithm (Euclidean distance, k=4) allowed clustering the 3kbp-regions into 4 groups: active chromatin (AC) enriched in H3K4me2/3, facultative heterochromatin (FH) enriched in H3K27me3, constitutive

heterochromatin (CH) enriched in H3K9me2 and undetermined (UND) depleted in all these 4 marks. The lengths and the genomic localization of the domains assigned to each of the 4 chromatin states were used to generate the plots in **Figure 1B-C** and in **Supplementary Figure S1A**.

Genome-wide chromosome simulations.

The chromosome polymer model. Molecular dynamics simulations of the diploid *A. thaliana* genome were run using the 30nm-fibre model (61), in which each bead hosts 3 kbp of DNA sequence and has a diameter of 30 nm. Each *A. thaliana* chromosome was represented as a chain of beads using the Kremer-Grest bead-spring model (62, 63) resulting in a fibre thickness of 30 nm and a persistence length of 150 nm (64) and avoiding chain crossings (**Supplementary methods**). The lengths of *A. thaliana* chromosomes (in bp and in models' beads) and the genomic locations of special sequences (NORs and centromeres) are reported in **Supplementary Table S1**.

Additional epigenomics-based short-range interactions were added to test how the attractions or repulsions between the *A. thaliana* chromatin states shape the chromosome organization. These interactions have been modelled using attractive or repulsive Lennard-Jones potentials of strengths 0.05, 0.50 and 1.00, where $k_B=1.38\times10^{-23}$ J/K is the Boltzmann constant, and T=298 K is the temperature of the system. Finally, the dynamics of the polymer model was simulated by integrating the (underdamped) Langevin equation of motion using LAMMPS (**Supplementary Methods**).

Single-chromosome preliminary simulations. Single-chromosome simulations were performed for chromosome 4 (Chr4) described as a chain of 6,195 beads (excluding the NOR4 to simplify). To enhance the statistics, we simulated at the same time 5 copies of Chr4 placed in a cubic simulation box (size 2.0 μm) with periodic boundary conditions (DNA density of 0.012 bp/nm^3 as used in previous works (29, 63)). To mimic a mitotic-like state, each model chromosome was initially prepared in an elongated solenoidal-like configuration (29), and the 5 copies were placed in a random, yet non-overlapping arrangement. For each parameter set, the dynamics of 10 independent trajectories were then simulated using LAMMPS (**Supplementary Methods**).

The genome-wide models. For genome-wide simulations, we prepared the initial conformations as (i) linear rod-like chromosomes, (ii) V-shaped chromosomes generated by linear pulling along the same direction, (iii) V-shaped chromosomes generated by linear pulling along radial directions. The procedures to generate the shapes of the chromosomes, to form the nucleolus by preconditioning the NORs arrangement, and to confine the chromosome models in a spherical nuclear environment are discussed in detail in **Supplementary Methods**. The initial conformations were used for the simulations in which the optimal settings of the epigenomic-based interactions were applied on a genome-wide scale.

KNOT engaged elements-driven steered molecular dynamics. 50 steered molecular dynamics simulations were performed to promote the spatial proximity between the KNOT engaged elements (KEEs) (42, 65) starting from the final snapshots of the optimal-model simulations. In particular, harmonics were applied between the central beads of the KEEs regions each spanning ~450 kbp. Briefly, the distances between the central beads of the KEEs were computed both *cis*- and *trans*-chromosome in all the 50 initial conformations and the closest bead pairs across all the snapshots were co-localized (**Supplementary Methods**) using the experimental FISH association rates (65) (20% of the KEE6-KEE1, 35% of the KEE5-KEE4, 66% of the KEE6-KEE3, and 16% of the KEE5-KEE10 pairs), or the average rate of 34% for all the other KEEs pairs.

Analysis of the polymer models.

Comparison with Hi-C data. Three Hi-C datasets for *A. thaliana* Col-0 seedlings were downloaded from the sequence read archive (SRA) (**Supplementary Table S2**) using *fastq-dump* (https://github.com/ncbi/sra-tools/wiki). Each experiment was processed through the TADbit pipeline (66) (https://github.com/3DGenomes/tadbit). Briefly, the pipeline consists of (i) Checking the quality of the FASTQ files; (ii) Mapping of the paired-end reads to the A. thaliana reference genome (release TAIR10 ftp://ftp.ensemblgenomes.org/pub/release-40/plants/fasta/arabidopsis_thaliana/dna/) using GEM (67) taking into account the DpnII restriction enzyme cut-site using fragment-based mapping (66); (iii) Filtering to remove non-informative reads using the following (default) TADbit filters: self-circle, dangling-ends, error,

extra-dangling-ends, duplicated and random-breaks (66); (iv) Merging of the datasets into a single one for the restriction enzyme DpnII; (v) Normalization of the merged datasets using the OneD (68) method at 3 kbp and 30 kbp resolution. Before merging the datasets (point (iv)), their mutual consistency was verified using the reproducibility score (R-score) (69). The obtained R-score values ranged between 0.56 and 0.84 indicating consistency between the merged datasets (69).

For each simulated configuration, contacts were computed using a cut-off distance of 200 nm which characterized roughly the spatial resolution of Hi-C experiments (70, 71). From these contacts, we then built contact maps for the single-chromosome (**Figure 2M-R**; **Supplementary Figure S3**) and genome-wide (**Figure 3D**, **3I**, and **3N**; **Figure 5I-J**; **Figure 6B-F**; **Supplementary Figure S6G-H**; **Supplementary Figure S9B-D**) cases. In the latter, we also estimated the average contact probability P(s) by averaging the predicted contact frequency over all the pairs of loci at the same genomic distance s (**Figure 3E**, **3J**, and **3O**). To compare visually predicted and experimental Hi-C data, the number of contacts in the models were re-scaled such that the average number of contacts at a genomic distance of 300kb (the number of bp in one Kuhn segment) equals the experimental one. Quantitative comparisons were made using the Spearman correlation coefficient (SCC) analysis applied to cis-chromosomal, genome-wide matrices and the P(s) (**Figure 2S-X**; **Figure 3F**, **3K**, and **3P**; **Supplementary Figure S2**, **S5** and **S9**).

Nuclear positioning of genomic regions. Radial positions of the beads for each epigenomic state were used to build the histogram of the number of beads per concentric nuclear shell of width 250 nm. Final bar plots (**Figure 4F-J**; **Figure 5F-H**; **Supplementary Figure S6E-F**; lower panels of **Supplementary Figures S7** and **S8**) were obtained by dividing the number of particles by the volume of each shell. The standard deviations per shell were computed as the standard error of the mean over the 50 replicates.

Number of distinct chromocentric regions. Each chromocenter was considered as a sphere (radius = the radius of gyration of the constitutive particles; centre = their centre of mass) (**Figure 4L**). The overlap between two spheres was computed using the formula in Weisstein, Eric W. "Sphere-Sphere Intersection." From MathWorld--A Wolfram Web Resource.

http://mathworld.wolfram.com/Sphere-SphereIntersection.html. The average number of distinct chromocenters was computed varying the overlap volume threshold between 0.0 and 1.0 every 0.1. The threshold of 0.4 corresponded to an average of 8.5 distinct chromocenters close to the experimental estimate of 8.6+/-0.2 (46).

RESULTS

Epigenomics-driven folding of *A. thaliana* chromosomes using polymer models.

In this study, we tested the hypothesis that epigenomics is a driving force of the genome structural organization in *A. thaliana*. To this end, we built polymer models of the chromosomes using beads of 30 nanometers (nm) hosting each 3 kilobase pairs (kbp) of chromatin (**Figure 1A**). Next, we used short-range attractive or repulsive interactions between 3kbp-regions defined by their epigenomic state and studied how these interactions shape the 3D organization genome-wide in conditions of density and confinement mimicking the nuclear environment.

Based on the enrichment in epigenomic marks (44, 45), we assigned to each 3kbp-region one of four chromatin states (36) (**Methods**). A total of 52% of the genome was assigned to active chromatin (AC) enriched in H3K4me2 and H3K4me3, 14% to facultative, polycomb-like heterochromatin (FH) decorated with H3K27me3, 14% to constitutive heterochromatin (CH) enriched in H3K9me2, and 12% to undetermined (UND) regions that were depleted in all the considered epigenomic marks (**Figure 1B** and **C**, and **Supplementary Figure S1**).

The remaining parts of the *A. thaliana* genome were assigned to two other genomic categories that we used as complementary to the epigenomic states. The nucleolar organizing regions (NORs), that are the constitutive sequences of the nucleolus (41, 49, 50), account for 6% of the genome and are localized in the small arms of chromosomes 2 and 4, called NOR2 and NOR4 respectively. The telomeres, that account for about 1% of the genome, are the initial and terminal ~150 kbp regions of each chromosome (**Figure 1C**, **Supplementary Figure S1B** and **D**, **Supplementary Table S1**). To account for the high concentrations of RNA and proteins within the nucleolus (41, 49, 50) and for the typically increased stiffness of

the telomeres (72), NORs and telomeric 3kbp-regions were modelled as thicker beads of diameter 132 nm (**Figure 1A** and **Supplementary methods**).

Excluding the NORs, the more extended epigenomic domains of ~400 kbp were assigned to constitutive heterochromatin (CH) (**Figure 1B**) and, consistently with previous analysis (58, 59), were localized at the chromocenter (centromeric and pericentromeric region) of each chromosome (**Figure 1C** and **Supplementary Figure S1A-E**). The genomic regions occupied by active chromatin and facultative heterochromatin were organized into many interspersed domains of shorter lengths (maximum 93 kbp for AC and 84 kbp for FH, and median 6 kbp for AC and 3 kbp for FH).

Single-chromosome analysis allows parametrizing the epigenomics-driven interactions.

To find the optimal epigenomics-driven model, we designed a strategy to minimize the amount of numerical calculation needed and yet get a good understanding of how the different parameters affect the final compliance with the experiments. We focussed initially on the folding of chromosome 4 as it is the shortest in *A. thaliana* (**Supplementary Table S1**) and neglecting for simplicity the nucleolar organizing region (NOR4). Hence, we simulated a toy-model with 5 copies of chromosome 4 with random initial placements and orientations in a cubic box with periodic boundary conditions at the typical DNA density (ρ=0.012 bp/nm^3) of the nuclear environment (29, 63) (**Methods**).

We tested different types of short-range interactions involving the epigenomic chromatin regions defined above: self-attraction (full circles in **Figure 2A-F** and **Supplementary Figure S2**) and repulsion (dashed lines in **Figure 2A-F** and **Supplementary Figure S2**). Unless specified, the model beads interact with an excluded volume that allows the fibre to maintain a thickness of 30 nm and to avoid chain crossing (**Methods**). Yet simple, these physical mechanisms effectively account for known interactions that have been shown to occur in the nucleus. For instance, the heterochromatin protein 1 (HP1) binds to regions with high repressive histone methylation (H3K9me2) (73, 74) and favours the segregation of constitutive heterochromatin in the nucleus and *in vitro* (73, 75). Building on this previous

knowledge, we applied effective repulsions between constitutive heterochromatin (CH) and the other epigenomic states in each of the explored cases (**Figure 2A-F** and **Methods**).

On top of the CH repulsions, we explored 6 possible different scenarios illustrated in **Figure 2A-F**. Namely, we tested the self-attraction of the active-chromatin (AC) regions (**Figure 2A**), the repulsions of the facultative heterochromatin (FH) with the AC and the undetermined regions (UND) (**Figure 2C**), and the mutual repulsions between AC, FH, and UND regions (**Figure 2E**). The other interaction sets were obtained from the previous ones adding the self-attraction of the constitutive-heterochromatin (CH) regions (**Figure 2B**, **2D**, and **2F**).

For each set of interactions, we used 3 values of interaction strength equal to 0.05, 0.50, or 1.00 k_BT. One k_BT typically represents an energy of the order of the thermal noise. The selected values of interaction strength allow sampling distinct scenarios in which each of the imposed interactions is 1/20th (0.05 k_BT), half (0.50 k_BT) or of the same order (1.00 k_BT) of the thermal noise. We simulated 10 independent trajectories of a few hours (30, 63) using Langevin dynamics (**Methods**) and obtained an ensemble of ~400 conformations per parameter set (**Figure 2G-L** for illustrative snapshots at the end of the simulations).

To select the optimal interaction model, we estimated predicted contact maps at 30 kbp resolution (**Figure 2M-R** and **Methods**) and computed the Spearman correlation coefficient (SCC) (76, 77) between predictions and the experimental Hi-C maps (44, 45) (**Figure 2S-X** and **Methods**).

The obtained SCC values were larger than 0.65 for all the tested interaction models (**Figure 2S-X**) indicating that the explored parameters allow capturing the overall arrangement of chromosome 4. These high correlations are mainly due to the formation of a segregated domain (**Figure 2M-R**) at the chromocenter, that, in the models, is favoured by the repulsive interactions between heterochromatin (CH) and other beads. The difference in SCC among the 6 different scenarios, that account for at most 0.19, is due to the additional interactions. For instance, the attractive interaction between constitutive heterochromatin (CH) beads (**Figure 2B**, **Figure 2D**, and **Figure 2F**) only minimally improved (1% higher SCC at most) the correlation with the Hi-C data, indicating that already the repulsive interactions involving CH

beads are sufficient to promote the segregation of the chromocenters favouring effective compaction of the CH regions.

Notably, we found that the SCCs obtained from the simulations with the weak strength (0.05 k_BT) were consistently higher than the others (**Figure 2S-X**). These trends are due to the fact that the intra-arm contact patterns of Hi-C maps made of strips (~100 kb thick) of mildly increased (or depleted) interactions are captured in the predicted contact maps. But, as the interaction strength increases, the separation between enriched and depleted strips becomes sharper with the effect of degrading the correlation with the Hi-C map (**Supplementary Figure S3A-C**).

The highest correlation value of 0.84 was obtained for the scenario where the weak repulsions (E_{CH-*}=0.05 k_BT) of constitutive heterochromatin (CH) regions was applied together with the weak self-attraction (E_{AC-AC}=0.05 k_BT) between active-chromatin (AC) regions (**Figure 2A**, **2G**, **2M**, and **2S**). The addition of the self-attraction between constitutive heterochromatin (**Figure 2B**, **2H**, **2N**, and **2T**) only marginally improved the results. The parsimonious/minimal set of interactions of the test-case in **Figure 2A** was then used to obtain genome-wide models.

Genome-wide models reveal an overall preferential V-shape for *A. thaliana* chromosomes.

To generate genome-wide models, we prepared each of the 10 model chromosomes (chromosomes 1 to 5 in 2 copies each, **Supplementary Table S1**) as ideal rod-like structures of stacked rosettes along the main axis (29, 63) to mimic a simplified shape of the mitotic chromosome (**Supplementary Figure S4A**). The positions and orientations of each chromosome were chosen randomly inside a sphere of diameter 5.0 micrometre (μm), that is the typical *A. thaliana* nucleus size (78).

From 50 independent replicates of these initial chromosome conformations (**Figure 3B**), we simulated a few hours of the full genome dynamics (63) applying the optimal set of parameters inferred from the single-chromosomes simulations (**Figure 3A**). To characterize the contact patterns of the obtained models (representative snapshot in **Figure 3C**), we computed the genome-wide contact map (**Figure 3D**) and the average probability of contact (P) as a function of the genomic distance (s) between genomic regions on a set of ~2,000 conformations and compared them with the

genome-wide interaction map and the P(s) obtained from Hi-C experiments (44, 45) (**Figure 3E** and **Methods**).

Models recovered the main large scale contact patterns of the Hi-C (**Figure 3D**). Chromosomes appear along the main diagonal as squares of much higher contacts than the trans-chromosome parts, indicating that the models capture the organization in distinct chromosome territories (41, 42, 44, 65).

Interestingly, the epigenomics-driven models capture also the contact enrichment between chromocenters and telomeres of different chromosomes indicating that the effective repulsions between CH and the other chromatin states recover both the segregation of chromocenters at the cis-chromosome scale and the effective trans-chromosome attraction between chromocenters (41, 42, 44–46, 52, 65).

We also found a discrepancy between the experimental and the predicted contact probabilities P(s) (**Figure 3E**). The experimental P(s) exhibits two regimes: at short and intermediate genomic distances (100 kbp < s < 10 Mbp) P(s) decays as $s^{-0.84}$, which is very well captured by the models. But, at larger genomic distances (s > 10 Mbp), corresponding to the typical range of inter-arm contacts, the observed increase of P(s) in Hi-C is missing in our prediction.

To quantify the similarities of the models with experiments, we computed the Spearman correlation coefficient between the genome-wide maps, the 5 cis-chromosome maps and the P(s) (**Figure 3F**) in Hi-C and in our predictions. The comparisons between contact maps resulted in significant SCC values. We found that the minimal SCC of 0.46 was obtained for the genome-wide contact maps, where the size of the compared samples is ~7,000,000, and that in the per-chromosome comparisons the SCCs were always larger than 0.70 (sample-size > 180,000). Confirming the visual impression, the prediction of the P(s) was only marginally accurate (SCC=0.42 for sample-size=1,014).

To account for the inter-arm increase of contacts in the Hi-C maps, we designed a completely novel strategy to precondition the chromosome models in V-shaped arrangements (**Figure 3G**). The preconditioning attempts to incorporate an effective memory of chromosome structure throughout the cell cycle. During anaphase chromosomes are pulled, centromere first, towards opposite poles of the mother cell (52, 79). This results in a V-shape organization for metacentric chromosomes 1, 3

and 5 and in hook-like structures for acrocentric chromosomes 2 and 4. Assuming that chromosomes exhibit inherent properties of long-polymers in dense or semi-dilute solutions (31, 32, 80) we hypothesise that chromosomes maintain an effective memory of these V-like shapes during interphase.

Next, we initially arranged each chromosome in the linear (rod-like) shape (**Supplementary Figure S4A**) and then pulled it by the kinetochore (centromere) with harmonic forces along parallel directions (**Supplementary Figure S4B**). To allow for the dragging of the entire chromosome structure, during the pulling process we pinned the chromosomes in a looped conformation using harmonic bonds bridging regions at a typical separation of ~40 kbp (14 model beads) (**Supplementary methods**).

We simulated 50 replicates of the system with V-shaped chromosomes using the optimal epigenomic-driven interactions (**Methods**) and characterized quantitatively the obtained conformations (representative snapshots in **Figure 3H**) computing the genome-wide contact map and the P(s) (**Figure 3I** and **3J**). Applying the SCC analysis to compare with Hi-C, we observed that preconditioning the chromosomes in V-shaped conformations allowed capturing qualitatively and quantitatively the behaviour of the P(s) (**Figures 3J** and **3K**). The results obtained for the comparison of the contact maps (**Figures 3K**) were also improved in the genome-wide case and for chromosomes 2 and 4, while for the others were the same (chromosome 3) or only marginally degraded (chromosomes 1 and 5).

Interestingly, we also tested the possible formation of V-shaped chromosomes from a radial chromosome pulling which is less biologically-founded (**Figures 3L-P**, **Supplementary Figure S4C**, and **Methods**). We found overall lower correlations with the Hi-C (**Figures 3P**). In particular, the SCC of the P(s) dropped from 0.86 for the parallel pulling case to 0.73 for the radial one.

The epigenomics-driven models capture the nuclear organization in *A. thaliana*. To further characterise the models obtained from the optimal set of parameters, we looked at the preferential nuclear location of the regions assigned to each epigenomic state (**Figure 4A-E**) and computed the distribution of their radial positions (**Figure 4F-J** and **Methods**). To disentangle which of the typical nuclear positioning was to attribute to the specific epigenomics-based interactions, we

designed and performed a reference set of simulations in which the initial V-shaped chromosome positioning and the NORs and telomeres attractions were maintained, but the other interactions were removed (network in **Supplementary Figure S5C**). The results of this variant system are shown in the histograms in **Figures 4F-J** in white colour as a term of comparison with the optimal interaction model whose results are shown in the characteristic colour of the epigenomic state.

Interestingly, we found that the nucleolus typically assumed a round shape with a radius around 1,250 nm and occupied the centre of the model nucleus (**Figure 4A** and **4F**). The telomeres tended to localize at the nucleolar periphery (**Figure 4B** and **4G**). These features are consistent with the reference model in which NORs and telomeres are involved in the same interactions. Notably, the constitutive heterochromatin (CH) domains typically occupied the outermost shell of the nucleus in the optimal model but were pushed more to the nuclear interior in the reference one (**Figure 4C** and **4H**), in which the CH repulsions are lost. The active-chromatin and the facultative heterochromatin also tended to a slightly more peripheral positioning than in the reference interaction model (**Figure 4D-E** and **4I-J**). Overall, these results are consistent with experimental evidence on the typical positioning of the nucleolus at the nuclear centre (41, 49, 50), of telomeres at the nucleolar periphery (42, 44–46, 65), and of heterochromatic regions at the nuclear periphery (46, 52).

Next, we tested whether the preferential locations of the nucleolus and heterochromatin are also consistent with the fact that the telomeres, and chromocenters of chromosomes 2 and 4, which host the NORs, associate with the nucleolus forming the so-called nucleolar-associated domains (NADs) (50). In *A. thaliana*, NADs correspond to repetitive elements that are transcriptionally silenced by repressive histone modifications and DNA methylation. To identify the predicted NADs in the nuclear models, we computed per each 3kbp-region (1 bead) in the models the number of contacts with the NORs particles within a distance cutoff of 200 nm (**Methods**). In agreement with the experiments (50), we found that the top 10% regions making contacts with the NORs particles are the telomeric regions of each chromosome and the short arms of chromosomes 2 and 4 (**Figure 4K**). As a consequence, also the chromocenters of chromosomes 2 and 4 are involved in

many contacts with the nucleolus and are typically found in a perinucleolar location in agreement with experimental data (46, 52).

Next, we tested whether the typical location of the heterochromatic regions at the nuclear periphery is also consistent with the experimental evidence that groups of chromocenters coalesce together in 8.6+/-0.2 distinct foci with a characteristic distribution (46). Specifically, in each snapshot of the trajectories, we considered the regions composing each of the 10 centromeres (as a proxy of the chromocenters, **Supplementary Table S1**) and associated to each of them a sphere centred at the centre of mass of the beads with a radius equal to their radius of gyration (**Figure 4L**). Per each chromocenters pair, we computed the overlap volume between the two representative spheres. To compare with experiments (46), we selected the threshold of the significant overlap to 0.4 so that the average number of distinct chromocenters in the model nuclei over the 50 replicates simulations is 8.5 that matches the average number measured experimentally (8.6+/-0.2). The correspondent distribution of chromocenters' numbers resembles the experimental one with all the predicted values per bin showing no significant differences with the experimental ones (**Figure 4M**).

NORs and heterochromatin interactions shape the nuclear organization in *A. thaliana*.

To test the role of each epigenomics-based interaction, we generated models for four variant cases in which we modified the interactions involving one chromatin state at a time. Specifically, we perturbed the optimal interaction model (**Figure 3A)** by first removing the self-attraction among NORs and telomeric 3kbp-regions (**Figure 5A** and **5C-D**), second removing the repulsions between constitutive heterochromatin beads and the other epigenomic states (**Figure 5B** and **5E**), third by removing the self-attraction between active chromatin regions (**ASupplementary Figure S6A** and **C**), and fourth by adding the self-attraction between facultative heterochromatin beads (**Supplementary Figure S6B** and **D**). Next, each of the four variants was compared to the optimal epigenomic model by considering the radial distributions of 3kbp-regions (**Figure 5F-H**, and **Supplementary Figure S6E-F**) and the genome-wide contact maps (**Figure 5I-J** and **Supplementary Figure S6G-H**).

The similarities with the Hi-C interaction maps were quantified for each of the variant systems using the SCC analysis (**Supplementary Figure S5D-G**).

Interestingly, we found that removing the self-attraction of the NORs and the telomeric beads causes the most dramatic nuclear rearrangements. The compact nucleolus was disrupted (**Figure 5C,** representative snapshot) and the NORs regions were spread over the entire nucleus, resulting in an enrichment of NORs beads at the nuclear periphery and a depletion at the centre with respect to the optimal interaction model (**Figure 5F**). The telomeres also lost their preferential perinucleolar positioning and relocalized in more peripheral shells of the nucleus (**Figure 5D** and **5G**). Furthermore, the perturbation of NORs interactions affected also the nuclear positioning of the constitutive heterochromatin (CH), active chromatin (AC) and facultative heterochromatin (FH) regions, that are found in more central nuclear positions despite their epigenomics-driven interactions were maintained in this perturbed system (**Supplementary Figure S7**). Interestingly, the large change in nuclear positioning has a marginal role in perturbing the contact patterns for this NORs' variant system. The corresponding genome-wide contact map, that does not include the NORs regions for consistency with the Hi-C interaction maps, appears to be visually very similar to the one obtained for the optimal interaction model (**Figure 5I**) and quantitatively correlates equally well with the Hi-C interaction maps (**Supplementary Figure S5D**).

The removal of the repulsive interactions between CH beads and the other epigenomic states (**Figure 5B**) had the effect to push the heterochromatic regions towards the nuclear centre so that CH beads are less probably found in the outermost nuclear shell than in the optimal interaction model (**Figure 5E** and **5H**). Notably, the CH perturbation also marginally affected the nuclear location of the other epigenomic (AC and FH) states by pushing them slightly towards the nuclear centre (**Supplementary Figure S8**). Interestingly, the main reverberation of the CH perturbation appears in the genome-wide contact map. Specifically, the signatures of the segregation of the centromeric regions are visually lost, and the trans-chromosome sections of the map are different from the correspondent parts in the optimal interaction case (**Figure 5J**). Quantitatively, the correlation of the model contact map and the Hi-C interaction map is, in fact, lower (SCC=0.42) than the

optimal interaction model (SCC=0.50), although the average contact probability as a function of the genomic separation, P(s), is captured accurately (SCC=0.95) (**Supplementary Figure S5E**).

The perturbations of the AC and FH interactions (**Supplementary Figure S6A-B**), that involve a sizeable fraction of the genome (52% and 14%, respectively) had only a negligible effect on both the radial positioning of the corresponding chromosome regions (**Supplementary Figure S6C-F**) and the genome-wide contact pattern (**Supplementary Figure S6G-H** and **Supplementary Figure S5F-G**).

The model plasticity allows recovering fine-scale structural properties: the KNOT Engaged Elements (KEEs) and the local polycomb-like domains.

To test whether adding specific sets of interactions (both epigenomics-driven or not) may help to recover structural properties at fine-scale without compromising the ones at large-scale, we studied more in detail the structural role of the KNOT engaged elements, KEEs (aka Interacting Heterochromatic Islands (IHIs)) (42, 65) and of the facultative, polycomb-like (FH) heterochromatin (**Figure 6** and **Supplementary Figure S9**). In particular, we tested whether it is possible to recover the formation of long-range interactions between the 10 KNOT Engaged Elements (aka IHIs) that had been identified in Hi-C contact maps of *A. thaliana* (42, 65). KEEs appear as strong cis- and trans-chromosome peaks in the Hi-C interaction maps. Notably, we found that the KEEs associated peaks are completely absent in the predictions of the optimal epigenomics-driven model (**Supplementary Figure S9A**) indicating that it is unlikely that such contacts can be promoted by epigenomics-driven interactions alone. In fact, the KEEs are not decorated in our analysis by a common epigenomic mark, and consistently with alternative ChIP-seq analysis (44, 59), that allow for even more than four epigenomic states, KEEs are usually not associated to a specific chromatin state (42).

Association rates of 4 KEEs' pairs (KEE6-KEE1 20%, KEE5-KEE4 35%, KEE6-KEE3 66%, KEE5-KEE10 16% with an average of 34%) were previously measured by Fluorescent In Situ Hybridization (FISH) (65), which showed an average of 34% co-localization of KEEs pair. To enforce their mutual spatial proximity, we applied long-range harmonics (both cis- and trans-chromosomes)

between the central beads of KEEs' pairs (**Methods**). To use the minimal set of harmonics and the minimal possible forces, we computed the distances between all the pairs of KEEs central beads (both in cis- and trans-chromosome) in the 50 final snapshots obtained from the optimal model simulations and ranked the pairs for increasing mutual distance. On the same 50 snapshots (representative snapshot in **Figure 3H**), we applied harmonics (**Methods**) between the closest 34% (or, when available, the specific FISH association rate (65)) of each KEEs pair to promote their spatial colocalization.

We found that the plasticity of the models allowed accommodating all the KEEs interactions and that the generated contact pattern around KEEs pairs was a cross appearing in the inter KEEs portions of the contact map (**Figure 6A**). This specific pattern was due to the applied constraints that bring into spatial proximity only the central beads. However, recovering the KEEs contacts largely affected the large-scale chromosome rearrangements as it is conveyed visually by the genome-wide contact map (**Figure 6B**) and quantitatively by the Spearman correlation with the Hi-C interaction map, that degrades both genome-wide and in each cis-chromosome parts with respect to the optimal interaction model (**Supplementary Figure S9D** and **Supplementary Figure S5H**).

Next, we focussed on local structural features involving the 162 clusters of genes enriched in the H3K27me3 polycomb-related histone mark (median length 7.5 kbp and maximum length 95 kbp) that have been identified in the entire *A. thaliana* genome (56). Typically these clusters form a local plaid pattern in the experimental Hi-C maps indicating the formation of interactions between many, yet not all of them. To illustrate this contact pattern, we focussed on a 4 Mbp region (chr4:6,700,000-10,700,000) (**Figure 6C**) centred around the longest gene cluster, the 95kb-long cluster-100 in Ref. (56). We observed that in the optimal interaction mode the FH regions are only involved in the effective repulsions with NORs and constitutive heterochromatin (**Figure 3A**). The optimal model is, as a matter of fact, not primed to capture the formation of local interaction domains between H3K27me3-enriched gene clusters (**Figure 6E**).

To test whether the structural models are sufficiently plastic and allow to recover the formation of the H3K27me3-enriched gene clusters, we performed simulations

increasing the interaction energy between FH beads to the maximum value used in this study (1.0 k_BT). On these simulations, we computed the model contact map (representative local portions in **Figure 6D** and **6F**), and the SCC analysis with the genome-wide Hi-C interaction map (**Supplementary Figure S5G**). Notably, we found that the addition of strong self-attraction allows recovering the formation of local interacting domains between H3K27me3 enriched gene-clusters (**Figure 6D** and **6F**) without affecting the large-scale chromosome organization that correlated with the Hi-C interaction map as good as the optimal interaction model (**Supplementary Figure S5G**).

DISCUSSION AND CONCLUSION

We studied how and to what extent epigenomics-driven interactions shape the structural organization of the *Arabidopsis thaliana* genome. For this purpose, we developed a novel strategy based on an underlying polymer model that, decorated with epigenomics-based interactions (attractions and repulsions) and simulated via molecular dynamics, allowed generating accurate genome-wide structures of the *A. thaliana* chromosomes coarse-grained at 3 kbp.

Overall, we found a constitutive organizational role for the attraction between the nucleolar organizing regions NOR2 and NOR4, and for the repulsions of the constitutive heterochromatin (CH) regions and the rest of the genome. Interestingly, these interactions, that are part of the optimal interaction model, allow recovering several established experimental results (**Figure 3** and **4**). Specifically, the formation and the central nuclear positioning of the nucleolus (41, 49, 50), the close positioning of NADs to the nucleolus itself (50), the peripheral positioning of the CH regions (46, 52, 81), and the coalescence of chromocenters in discrete *foci* (42, 46, 65) were all recapitulated in our models. Importantly, these accurate predictions are lost when we remove separately the NORs self-attraction (**Figure 5** and **Supplementary Figure S7**) or the CH repulsions (**Supplementary Figure S8**).

The major role of nucleolus and centromeres to shape the nuclear organization in *A. thaliana* is consistent with previous findings from genome modelling (57), that we largely extend by providing mechanistic insight. We modelled the formation of the

nucleolus by the aggregation of the self-attractive constitutive NORs regions and by preconditioning them at the nuclear centre. We also tested that the NOR self-attractions are essential to maintain both a compact and central nucleolus (**Figure 5**) implying that the preconditioning and non-specific interactions, such as the depletion effect which may act due to the different size of the NOR beads, are not enough to achieve accurate structural organization. Our computational protocol for the formation of the nucleolus is also one of the first attempts of its kind in the modelling of the 3D genome organization higher eukaryotes. The only exception is yeast in which the rDNA sequence on chromosome XII has been modelled with an effective repulsion (82) or with *ad hoc* confinements (83, 84).

Our findings also reveal that the segregation of the chromocenters, their preferential positioning at the nuclear periphery, and their association in discrete clusters can be explained by epigenomics-driven effective repulsions of the constitutive heterochromatin with the other epigenomic states. In *A. thaliana*, it is known that the nuclear envelope hosts the nucleoskeleton (85), a peripheral matrix that is functionally comparable to the lamina in animal cells. It has been demonstrated that the proteins *crwn*1 in presence of *crwn4* and non-CG DNA methylation (85, 86) can bridge to the nucleoskeleton genomic regions, called Plant Lamina-Associated Domains (PLADs), in analogy with the LADs in animals (87, 88). PLADs are enriched in repressive chromatin marks and silenced chromatin but don't show a perfect correspondence with heterochromatin, suggesting that other factors, such as the epigenomics-based interactions proposed here, may aid the recruitment and the dynamical tethering of the chromocenters at the periphery. This feature of *A. thaliana* may be a difference with the genome organization in mammals in which the tethering of heterochromatin to the nuclear membrane via Lamin proteins has been shown to be essential for the recruitment and the tethering of heterochromatin at the nuclear periphery (89–91).

Together with NORs and CH interactions, another important finding of our study is that different initial shapes of chromosomes have a huge impact in recovering experimental evidence. We showed here that preconditioning the chromosome structures in a V-shape state, as expected for (sub)metacentric chromosomes, dramatically improves the description of the contact probability vs. the genomic

distance, P(s) (**Figure 3I-J**). This finding is to ascribe to topological constraints that allow long polymers (that are viable models for chromosomes (92)) keeping a partial memory of their initial arrangements over long timescales (29, 32, 80). The models allow discerning that the V-shapes obtained from the parallel (not radial) pulling of all chromosomes by the centromeres generate the most accurate models (**Figure 3K** and **3P**). Interestingly, our optimal pulling protocol resembles to some extent the large-scale dynamics during cell division in *A. thaliana* when the chromosomes of each daughter cell, after the first transient dynamics, move in parallel, centromere first, towards opposite poles of the mother cell (52, 79). We also wish to point out that we gathered this insight by analysing the P(s) from the Hi-C datasets. This fact is a clear example that the Hi-C contact patterns, once they are properly interpreted, can inform on the large scale chromosomes organization and that 3D modelling approaches offer a viable bridge to contextualize and quantitatively reconcile imaging and Hi-C results (70, 93). It is likely that this partial memory of the initial V-shape applies to other species with (sub)metacentric chromosomes like humans and flies where P(s) also exhibits an increase at genomic scales corresponding to inter-arm contacts (17, 94, 95).

Interestingly, the optimal interaction model we found is largely consistent with known weak (~0.05 k_BT) protein- and RNA-mediated interactions which may shape the chromatin structure *in vivo*. Specifically, the formation of the nucleolus by the attraction of the NORs in chromosome 2 and 4 may suggest an architectural role for ribosomal RNA (rRNA), RNA Polymerase I, and transcription factors that are enriched at the nucleolus (96–98). The repulsion of constitutive heterochromatin (CH) is consistent with the evidence that the heterochromatin complex 1 (HP1) binds to repressive histone marks (e.g. H3K9me2) and possibly forms insoluble protein droplets (75) that effectively increase the local chromatin volume. Similarly, the self-attraction of active chromatin (AC) could be justified by the binding of RNA PolII to active genes priming a similar micro-phase separation phenomenon (99, 100).

Interestingly, comparably weak epigenomic-driven interactions have been found in similar studies on *D. melanogaster* (37) and humans (33, 35, 74, 101–103). In the latter, the chromatin states are linearly organized into large (~100 kbp) blocks (104, 105) that concur to the formation of chromatin compartments in humans and TADs in

D. melanogaster. However, in *A. thaliana* the linear organization of the epigenomic states (**Figure 1A** and **Supplementary Figure S1**) (44, 58, 59) is characterized by small domains (median ~10kb) interspersed along all chromosomes, that may explain why we do not observe strong epigenomics-related compartments or TADs in *A. thaliana* (42, 44, 45, 65).

Additionally, the optimal models presented a degree of plasticity that allowed enforcing and satisfying the long-range contacts between pairs of KNOT Engaged Elements (KEEs). This mechanism might result from the molecular action of nuclear myosins that have been shown to promote long-range genomic contacts in mammals (106–108). However, we found in these simulations overall lower correlations between model contact patterns and Hi-C (**Figure 6**). This result suggests that the formation of KEEs interactions cannot be modelled by long-range harmonics applied on the optimal models, but has to be ascribed to alternative mechanisms. We may speculate, for instance, possible tethering of all (or part of) the KEEs to nuclear landmarks, as it is the case of the centromeres in yeast that are attached to the spindle pole body via microtubules (109). Also, short-range interactions could promote KEEs contacts, but, to be properly described using polymer modelling, they need a specific preconditioning procedure, such as the ones applied in this work for the nucleolus formation.

Interestingly, relatively strong (1 k_BT) short-range self-attraction between facultative-heterochromatin FH regions allow reproducing local contact patterns of the Hi-C maps (**Figure 6**). Specifically, in these simulations, the local interaction pattern between gene clusters enriched in H3K27me3 histone mark is recovered and minimally affects the correlations with Hi-C contact patterns. This finding suggests that we could recapitulate structural features at the scale of a few hundreds of kilobases, that are close to the limit of the model coarse-graining (~300 kb).

In conclusion, we show that using polymer models and epigenomics-driven interactions it is possible to predict the genome organization of *A. thaliana* and to discern the crucial role of NORs and heterochromatin in shaping its 3D genome. Additionally, we demonstrate that within the same modelling framework fine-scale genomic features, such as H3K27me3-enriched gene clusters and KEEs, can be quantitatively tested. Our fine-grained analysis unveils that our approach can also be

used to test reliably and quantitatively local genomic structural features (close to the coarse-graining limit), and also demonstrates that polymer modelling can robustly propose or rule out possible mechanisms underlying the formation of the contact patterns by verifying simultaneously their effect at large and local genomic scales. The computational modelling introduced here for *A. thaliana* will help to unravel the mechanisms behind the genomic organization not only in other complex plant species such as wheat and rice but also in many eukaryotes in which the nucleolus and heterochromatin are highly conserved elements.

FIGURES CAPTIONS

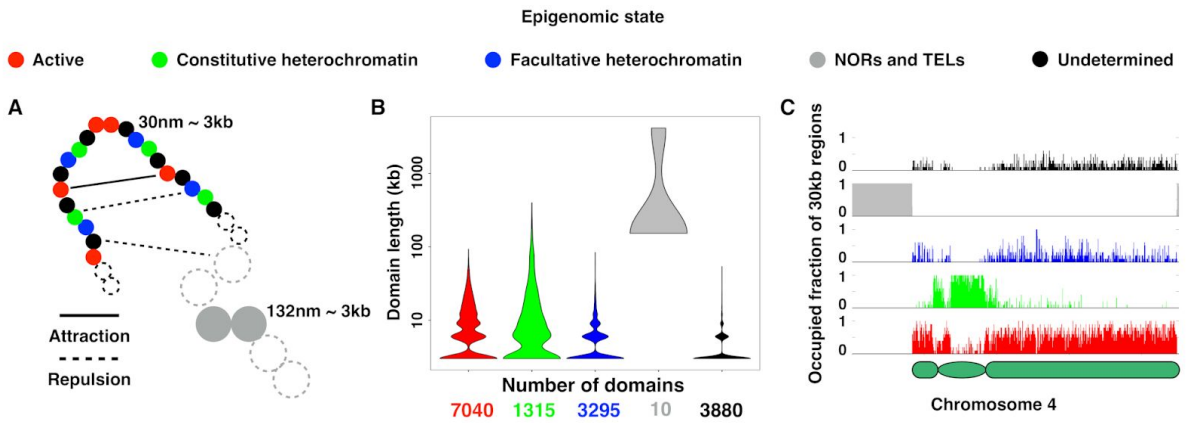

Figure 1. Epigenomics-driven co-polymer models of *A. thaliana* chromosomes. **(A)** Scheme of the polymer model. Chromosomes are modelled as self-avoiding bead-spring chains where each monomer represents a 3kbp-portion of chromatin and is characterized by its epigenomic state: active (red), constitutive heterochromatin (green), facultative heterochromatin (blue), NORs and telomeres (grey), and undetermined (black). Attractive or repulsive short-range interactions account for epigenomics-driven relationships between beads. **(B)** Distributions of the genomic length spanned by individual epigenomic domains (bottom: total number of domains per state). Each violin plot shows the density of the points smoothed with a Gaussian kernel with the standard parameters of R *geom_violin* function (110). **(C)** Profiles of each chromatin state along chromosome 4. Each profile is binned at 30 kbp and the height of the bars indicates the fraction of the 30kbp-bin occupied by 3kbp-regions of the corresponding chromatin state.

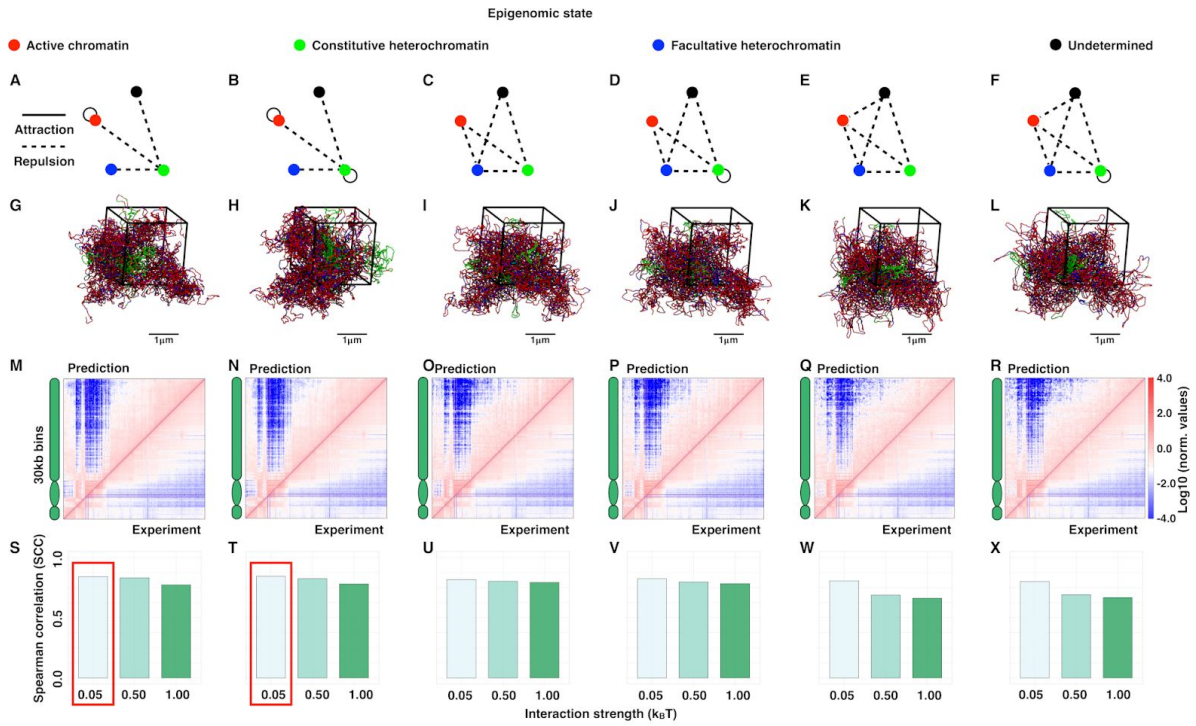

Figure 2. Parametrization of epigenomics-based interactions. **(A-F)** Networks representing the investigated sets of epigenomics-driven interactions. A link between two nodes represents a specific interaction. We show here results when all the strengths are equal to 0.05, 0.50 and 1.0 k_BT. Other combinations are presented in **Supplementary Figure S2**. **(G-L)** Illustrative snapshots of conformations obtained for each interaction network when all the strengths of interaction are E=0.05 k_BT. Particles are coloured depending on their epigenomic state. These and other graphical representations of model chromosomes were rendered with the VMD graphical package (111). **(M-R)** Predicted contact maps for the six simulated interactions sets (top left triangles, all E=0.05 k_BT) are shown together with the cis-chromosome 4 Hi-C maps (bottom right triangles). **(S-X)** The Spearman correlation analysis between the experimental and predicted contact maps (**Methods**). Red boxes highlight the optimal cases.

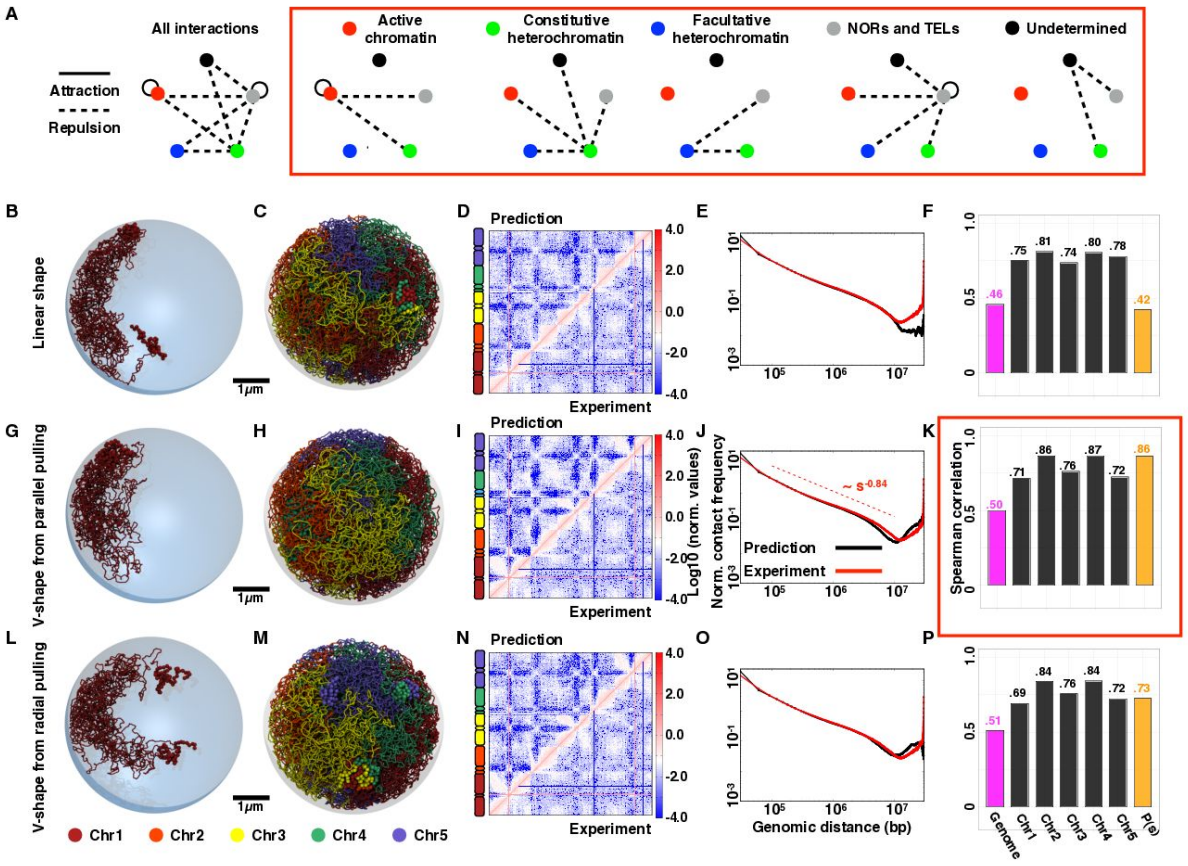

Figure 3. Genome-wide simulations: exploring the optimal epigenomics-based interactions and the effects of initial conformation. **(A)** Network of physical interactions used in the genome-wide simulations. In the red rectangle, the network is decomposed to highlight the interactions of each chromatin state. **(B-P)** Results of the genome-wide simulations for three alternative initial conformations: linear **(B-F)**, V-shape from parallel pulling **(G-K)**, and V-shape from radial pulling **(L-P)**. **(B**, **G**, **L)** Examples of initial (for a copy of chromosome 1) and **(C**, **H**, **M)** final (for all chromosomes) conformations. **(D**, **I**, **N)** Predicted genome-wide contact maps (top left triangles) together with the corresponding experimental Hi-C map (bottom right triangles). **(E**, **J**, **O)** Average intra-chromosome contact probability P vs genomic distance s computed from simulations (black curve) and from Hi-C (red curve). **(F**, **K**, **P)** Spearman correlation coefficients (SCC) computed to compare the models and the Hi-C data from genome-wide maps (magenta), cis-chromosome matrices (black), and P(s) (orange). The red box highlights the optimal case.

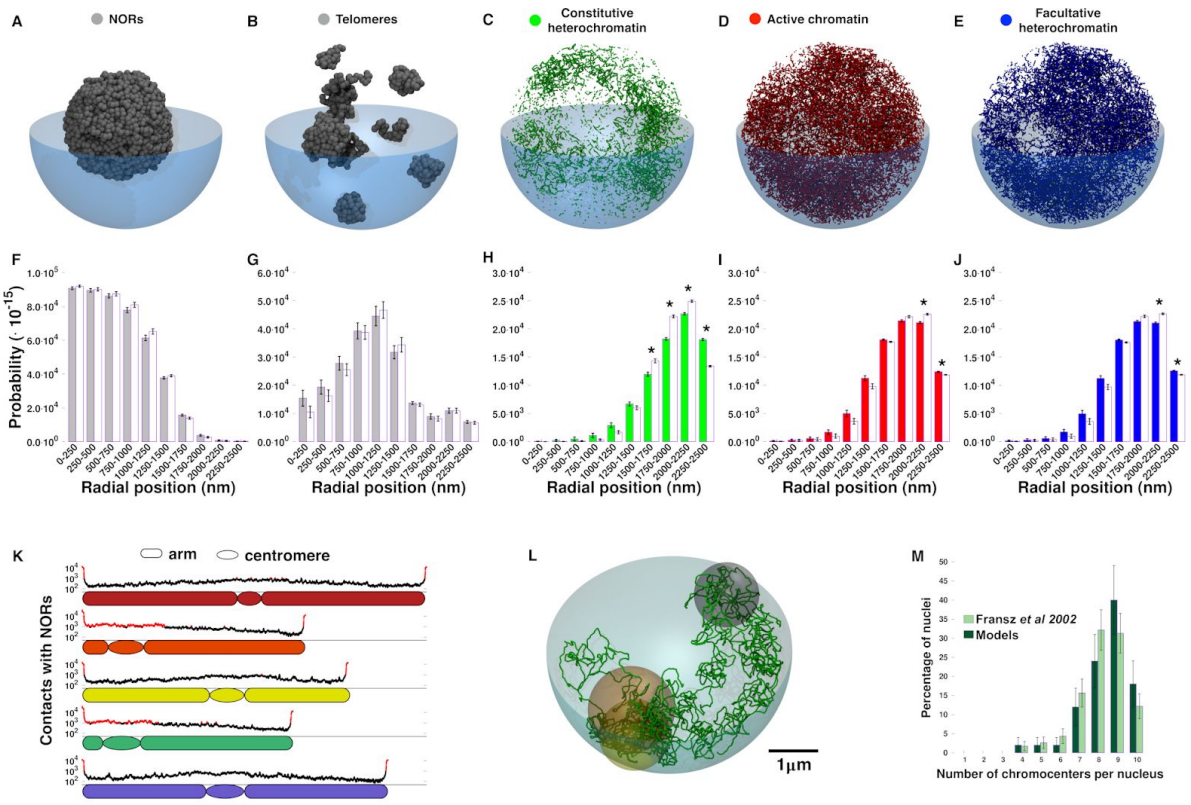

Figure 4. Nuclear positioning of the epigenomic states. **(A-E)** Representative snapshots of the nuclear localization of 3kbp-beads for each epigenomic state. **(F-J)** Probability to find a bead in concentric shells of the nucleus for each epigenomic state for the optimal interaction model (**Figure 3A**) (coloured bars). White bars illustrate the results of a null model (**Supplementary Figure S5C**) where all but NORs and telomeres interactions are switched off. The significantly enriched/depleted shells with respect to the null model (Two-sided Wilcoxon statistical test with p-value<0.0001) are marked with asterisks (**Methods**). **(K)** Predicted number of contacts within 200 nm with NORs particles along the different chromosomes. The top 10% of the contacting regions are highlighted in red. **(L)** Each group of centromeric beads per chromosome is represented by a sphere (radius = the radius of gyration of the constitutive particles; centre = their centre of mass). Spheres with a volume overlap larger than 40% the volume of the smaller sphere are part of the same focus. **(M)** Number of distinct centromeric foci per simulated conformation (dark green bars) and per experimental single cell (46) (light green bars). Error bars were computed as the square root of the average value under the hypothesis of a Poissonian distribution. For each bin, we tested if the

predicted average frequency is similar to the observed experimental counts (null hypothesis) by computing the p-value of the predictions assuming Poisson distribution for experiments. All p-values were higher than 0.02 making impossible to reject the null hypothesis.

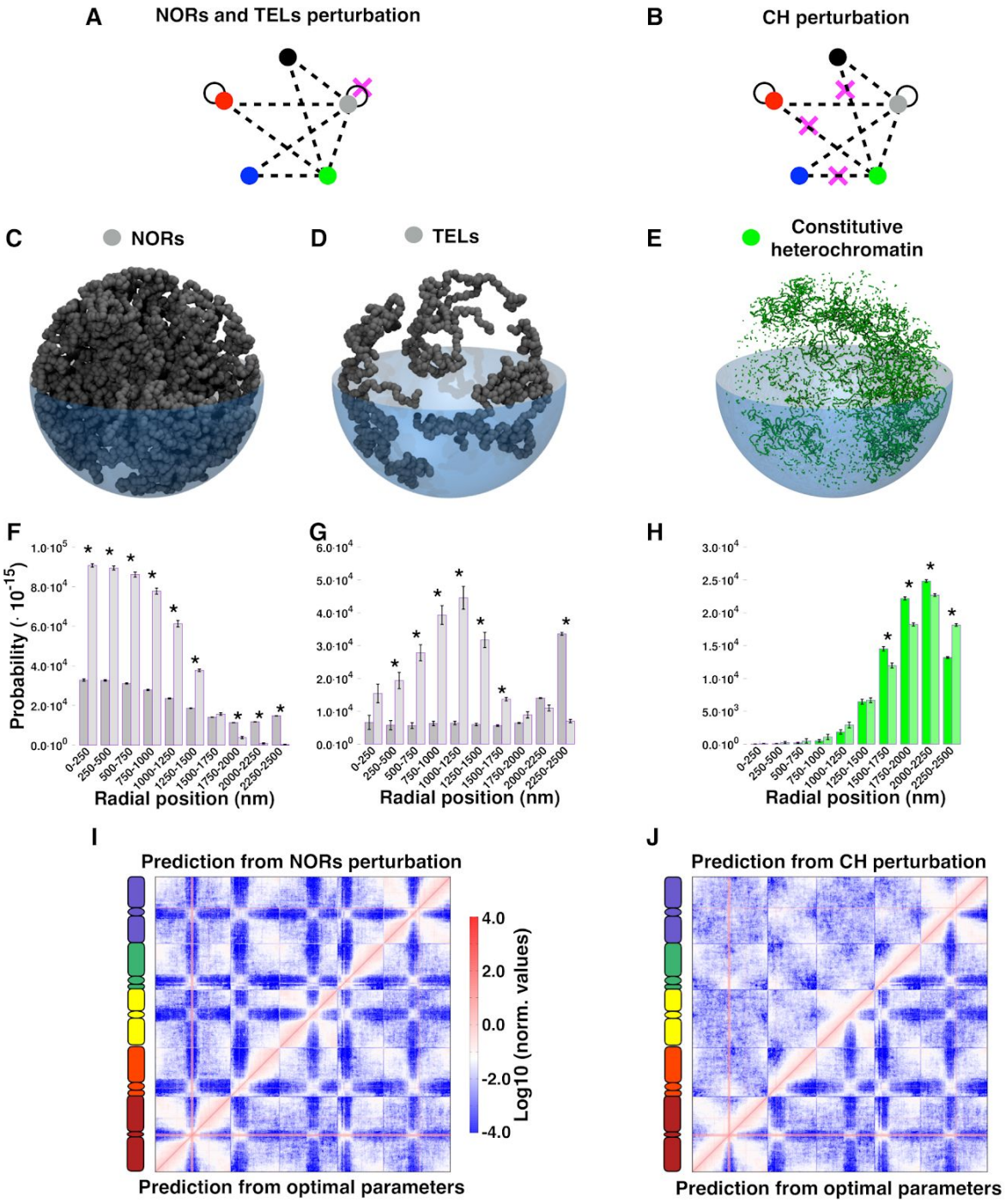

Figure 5. NORs and constitutive heterochromatin shape the *A. thaliana* nuclear organization. **(A-B)** Perturbed interaction networks. The interactions that are removed from the optimal case are crossed in magenta. **(C-E)** Illustrative snapshots for NOR (**C**) and telomeric (**D**) beads in the perturbed system shown in (**A**). (**E**) As in (**C, D**) but for CH beads in the scenario shown in (**B**). **(G-H)** Distributions of the radial positions of the 3kbp-regions in the perturbed systems (dark colour) compared to the

optimal interaction model (light colour). Significant differences (two-sided Wilcoxon test p-value<0.0001) are marked with asterisks. **(I-J)** Genome-wide contact map for the perturbed cases (top left triangles) vs maps obtained from the optimal interaction model (bottom right triangles).

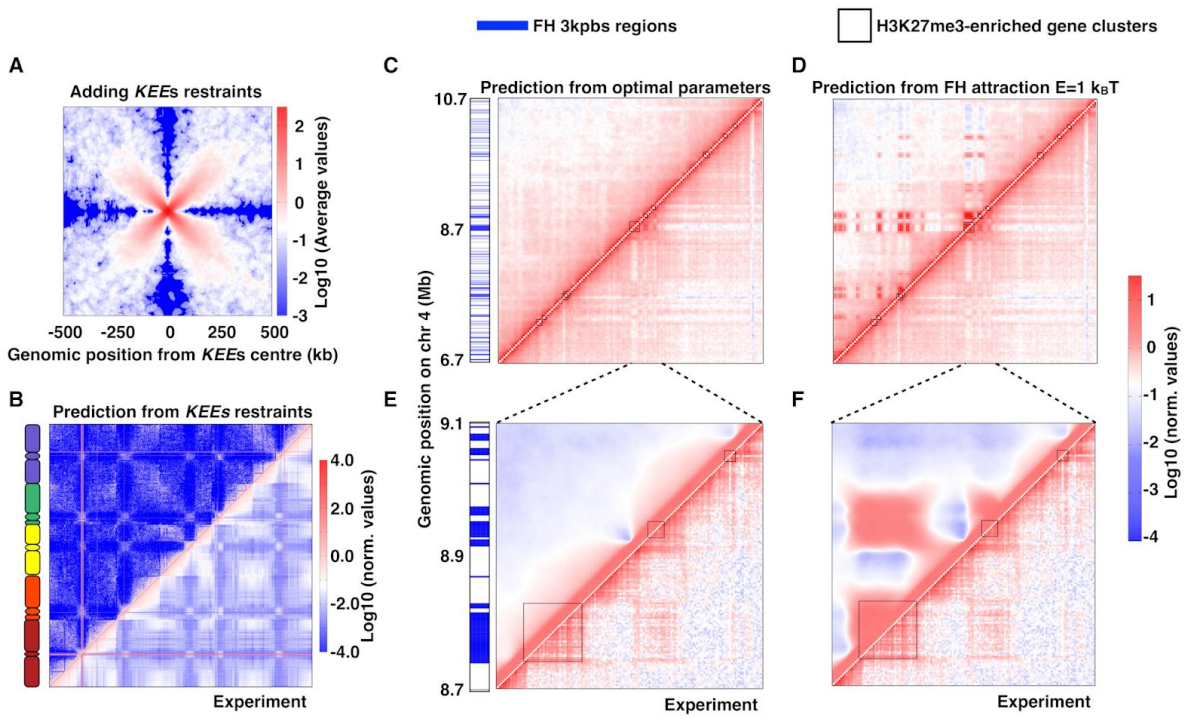

Figure 6. Plasticity of the optimal models in response to long-range and local interactions. (A) Average contact map of a 1Mbp-region around the KNOT Engaged Elements (KEEs) for the KEEs-restrained models. **(B)** Genome-wide contact maps in the KEEs-restrained case (top left triangle) and from experiments (bottom right triangle). **(C-D)** Predicted (top left triangles) vs experimental (bottom right triangles) contact maps at 30 kbp resolution in the chr4:6,700,000-10,700,000 bp region for the optimal set of parameters used in **Figures 3** and **4** (**C**) or the optimal set complemented with strong self-attraction (1 k_BT) between polycomb-like beads (**D**). **(E-F)** Zoomed views of **(C-D)** around the largest gene cluster (cluster 100 of Ref. (56)) (chr4:8,668,000-9,109,000 bp at 3 kb resolution). Black squares show the positions and extents of the gene clusters enriched in H3K27me3 mark (56). On the left of each map, blue lines indicate the positions of polycomb-like beads.

DATA AVAILABILITY

The Hi-C datasets analysed during the current study are available in the Sequence Read Archive (SRA) repository with accession numbers SRR1029605 from Ref. (44), SRR2626429, SRR2626163 from Ref. (45). Epigenomic data were extracted from the Supplementary Table 4 of Ref. (44). All LAMMPS, Bash, R and Python in-house scripts for simulations and data analysis used for this study will be available upon publication.

ACKNOWLEDGMENT

We are grateful to the members of the Marti-Renom and Jost labs, and to Paula Soler-Vila for useful discussions.

FUNDING

This research was partially funded by the European Union's H2020 Framework Programme through the ERC [grant agreement 609989 to MAM-R]. We also acknowledge the support of Spanish Ministry of Science and Innovation through BFU2017-85926-P to MAM-R CRG thanks the support of the Spanish Ministry of Science and Innovation to the EMBL partnership, the 'Centro de Excelencia Severo Ochoa 2013-2017' [SEV-2012-0208], the CERCA Programme/Generalitat de Catalunya, Spanish Ministry of Science and Innovation through the Instituto de Salud Carlos III, the Generalitat de Catalunya through Departament de Salut and Departament d'Empresa i Coneixement and the Co-financing by the Spanish Ministry of Science and Innovation with funds from the European Regional Development Fund (ERDF) corresponding to the 2014-2020 Smart Growth Operating Program. DJ acknowledges Agence Nationale de la Recherche [ANR-18-CE12-0006-03, ANR-18-CE45-0022-01] for funding. HWN acknowledges support from the Royal Society [University Research Fellowship UF160138]. This work was supported by an STSM Grant from COST Action CA17139.

CONFLICT OF INTEREST

None declared.

REFERENCES

1. Misteli,T. (2007) Beyond the Sequence: Cellular Organization of Genome Function. *Cell*, **128**, 787–800.

2. Gibcus,J.H. and Dekker,J. (2013) The Hierarchy of the 3D Genome. *Molecular Cell*, **49**, 773–782.

3. Bonev,B. and Cavalli,G. (2016) Organization and function of the 3D genome. *Nature Reviews Genetics*, **17**, 661–678.

4. Sexton,T. and Cavalli,G. (2015) The role of chromosome domains in shaping the functional genome. *Cell*, **160**, 1049–1059.

5. Dekker,J. and Mirny,L. (2016) The 3D Genome as Moderator of Chromosomal Communication. *Cell*, **164**, 1110–1121.

6. Bonev,B., Mendelson Cohen,N., Szabo,Q., Fritsch,L., Papadopoulos,G.L., Lubling,Y., Xu,X., Lv,X., Hugnot,J.-P., Tanay,A., *et al.* (2017) Multiscale 3D Genome Rewiring during Mouse Neural Development. *Cell*, **171**, 557–572.e24.

7. Stadhouders,R., Vidal,E., Serra,F., Di Stefano,B., Le Dily,F., Quilez,J., Gomez,A., Collombet,S., Berenguer,C., Cuartero,Y., *et al.* (2018) Transcription factors orchestrate dynamic interplay between genome topology and gene regulation during cell reprogramming. *Nat. Genet.*, **50**, 238–249.

8. Paulsen,J., Liyakat Ali,T.M., Nekrasov,M., Delbarre,E., Baudement,M.-O., Kurscheid,S., Tremethick,D. and Collas,P. (2019) Long-range interactions between topologically associating domains shape the four-dimensional genome during differentiation. *Nat. Genet.*, **51**, 835–843.

9. Dixon,J.R., Jung,I., Selvaraj,S., Shen,Y., Antosiewicz-Bourget,J.E., Lee,A.Y., Ye,Z., Kim,A., Rajagopal,N., Xie,W., *et al.* (2015) Chromatin architecture reorganization during stem cell differentiation. *Nature*, **518**, 331–336.

10. Zheng,H. and Xie,W. (2019) The role of 3D genome organization in development

and cell differentiation. *Nat. Rev. Mol. Cell Biol.*, **20**, 535–550.

11. Dekker,J., Rippe,K., Dekker,M. and Kleckner,N. (2002) Capturing chromosome conformation. *Science*, **295**, 1306–1311.

12. Cremer,T. and Cremer,C. (2001) Chromosome territories, nuclear architecture and gene regulation in mammalian cells. *Nature Reviews Genetics*, **2**, 292–301.

13. Boyle,S., Gilchrist,S., Bridger,J.M., Mahy,N.L., Ellis,J.A. and Bickmore,W.A. (2001) The spatial organization of human chromosomes within the nuclei of normal and emerin-mutant cells. *Hum. Mol. Genet.*, **10**, 211–219.

14. Bolzer,A., Kreth,G., Solovei,I., Koehler,D., Saracoglu,K., Fauth,C., Müller,S., Eils,R., Cremer,C., Speicher,M.R., *et al.* (2005) Three-dimensional maps of all chromosomes in human male fibroblast nuclei and prometaphase rosettes. *PLoS Biol.*, **3**, e157.

15. Branco,M.R. and Pombo,A. (2006) Intermingling of chromosome territories in interphase suggests role in translocations and transcription-dependent associations. *PLoS Biol.*, **4**, e138.

16. Lieberman-Aiden,E., van Berkum,N.L., Williams,L., Imakaev,M., Ragoczy,T., Telling,A., Amit,I., Lajoie,B.R., Sabo,P.J., Dorschner,M.O., *et al.* (2009) Comprehensive mapping of long-range interactions reveals folding principles of the human genome. *Science*, **326**, 289–293.

17. Sexton,T., Yaffe,E., Kenigsberg,E., Bantignies,F., Leblanc,B., Hoichman,M., Parrinello,H., Tanay,A. and Cavalli,G. (2012) Three-dimensional folding and functional organization principles of the Drosophila genome. *Cell*, **148**, 458–472.

18. Wang,S., Su,J.-H., Beliveau,B.J., Bintu,B., Moffitt,J.R., Wu,C.-T. and Zhuang,X. (2016) Spatial organization of chromatin domains and compartments in single chromosomes. *Science*, **353**, 598–602.

19. Imakaev,M., Fudenberg,G., McCord,R.P., Naumova,N., Goloborodko,A., Lajoie,B.R., Dekker,J. and Mirny,L.A. (2012) Iterative correction of Hi-C data

reveals hallmarks of chromosome organization. *Nat. Methods*, **9**, 999–1003.

20. Rao,S.S.P., Huntley,M.H., Durand,N.C., Stamenova,E.K., Bochkov,I.D., Robinson,J.T., Sanborn,A.L., Machol,I., Omer,A.D., Lander,E.S., *et al.* (2014) A 3D map of the human genome at kilobase resolution reveals principles of chromatin looping. *Cell*, **159**, 1665–1680.

21. Boettiger,A.N., Bintu,B., Moffitt,J.R., Wang,S., Beliveau,B.J., Fudenberg,G., Imakaev,M., Mirny,L.A., Wu,C.-T. and Zhuang,X. (2016) Super-resolution imaging reveals distinct chromatin folding for different epigenetic states. *Nature*, **529**, 418–422.

22. Xu,J., Ma,H., Jin,J., Uttam,S., Fu,R., Huang,Y. and Liu,Y. Super-Resolution Imaging of Higher-Order Chromatin Structures at Different Epigenetic States in Single Mammalian Cells. *SSRN Electronic Journal*, 10.2139/ssrn.3155874.

23. Dixon,J.R., Selvaraj,S., Yue,F., Kim,A., Li,Y., Shen,Y., Hu,M., Liu,J.S. and Ren,B. (2012) Topological domains in mammalian genomes identified by analysis of chromatin interactions. *Nature*, **485**, 376–380.

24. Nora,E.P., Lajoie,B.R., Schulz,E.G., Giorgetti,L., Okamoto,I., Servant,N., Piolot,T., van Berkum,N.L., Meisig,J., Sedat,J., *et al.* (2012) Spatial partitioning of the regulatory landscape of the X-inactivation centre. *Nature*, **485**, 381–385.

25. Bintu,B., Mateo,L.J., Su,J.-H., Sinnott-Armstrong,N.A., Parker,M., Kinrot,S., Yamaya,K., Boettiger,A.N. and Zhuang,X. (2018) Super-resolution chromatin tracing reveals domains and cooperative interactions in single cells. *Science*, **362**.

26. Szabo,Q., Jost,D., Chang,J.-M., Cattoni,D.I., Papadopoulos,G.L., Bonev,B., Sexton,T., Gurgo,J., Jacquier,C., Nollmann,M., *et al.* (2018) TADs are 3D structural units of higher-order chromosome organization in. *Sci Adv*, **4**, eaar8082.

27. Le Dily,F., Vidal,E., Cuartero,Y., Quilez,J., Nacht,A.S., Vicent,G.P.,

Carbonell-Caballero,J., Sharma,P., Villanueva-Cañas,J.L., Ferrari,R., *et al.* (2019) Hormone-control regions mediate steroid receptor-dependent genome organization. *Genome Res.*, **29**, 29–39.

28. Szabo,Q., Bantignies,F. and Cavalli,G. (2019) Principles of genome folding into topologically associating domains. *Science Advances*, **5**, eaaw1668.

29. Rosa,A. and Everaers,R. (2008) Structure and dynamics of interphase chromosomes. *PLoS Comput. Biol.*, **4**, e1000153.

30. Rosa,A., Becker,N.B. and Everaers,R. (2010) Looping Probabilities in Model Interphase Chromosomes. *Biophysical Journal*, **98**, 2410–2419.

31. Vettorel,T., Grosberg,A.Y. and Kremer,K. (2009) Statistics of polymer rings in the melt: a numerical simulation study. *Phys. Biol.*, **6**, 025013.

32. Halverson,J.D., Smrek,J., Kremer,K. and Grosberg,A.Y. (2014) From a melt of rings to chromosome territories: the role of topological constraints in genome folding. *Rep. Prog. Phys.*, **77**, 022601.

33. Brackley,C.A., Johnson,J., Kelly,S., Cook,P.R. and Marenduzzo,D. (2016) Simulated binding of transcription factors to active and inactive regions folds human chromosomes into loops, rosettes and topological domains. *Nucleic Acids Res.*, **44**, 3503–3512.

34. Pierro,M.D., Di Pierro,M., Zhang,B., Aiden,E.L., Wolynes,P.G. and Onuchic,J.N. (2016) Transferable model for chromosome architecture. *Proceedings of the National Academy of Sciences*, **113**, 12168–12173.

35. Di Pierro,M., Cheng,R.R., Lieberman Aiden,E., Wolynes,P.G. and Onuchic,J.N. (2017) De novo prediction of human chromosome structures: Epigenetic marking patterns encode genome architecture. *Proc. Natl. Acad. Sci. U. S. A.*, **114**, 12126–12131.

36. Jost,D., Carrivain,P., Cavalli,G. and Vaillant,C. (2014) Modeling epigenome folding: formation and dynamics of topologically associated chromatin domains.

Nucleic Acids Res., **42**, 9553–9561.

37. Ghosh,S.K. and Jost,D. (2018) How epigenome drives chromatin folding and dynamics, insights from efficient coarse-grained models of chromosomes. *PLoS Comput. Biol.*, **14**, e1006159.

38. Sanborn,A.L., Rao,S.S.P., Huang,S.-C., Durand,N.C., Huntley,M.H., Jewett,A.I., Bochkov,I.D., Chinnappan,D., Cutkosky,A., Li,J., *et al.* (2015) Chromatin extrusion explains key features of loop and domain formation in wild-type and engineered genomes. *Proc. Natl. Acad. Sci. U. S. A.*, **112**, E6456–65.

39. Fudenberg,G., Imakaev,M., Lu,C., Goloborodko,A., Abdennur,N. and Mirny,L.A. (2016) Formation of Chromosomal Domains by Loop Extrusion. *Cell Rep.*, **15**, 2038–2049.

40. Brackley,C.A., Johnson,J., Michieletto,D., Morozov,A.N., Nicodemi,M., Cook,P.R. and Marenduzzo,D. (2017) Nonequilibrium Chromosome Looping via Molecular Slip Links. *Phys. Rev. Lett.*, **119**, 138101.

41. Pecinka,A., Schubert,V., Meister,A., Kreth,G., Klatte,M., Lysak,M.A., Fuchs,J. and Schubert,I. (2004) Chromosome territory arrangement and homologous pairing in nuclei of Arabidopsis thaliana are predominantly random except for NOR-bearing chromosomes. *Chromosoma*, **113**, 258–269.

42. Feng,S., Cokus,S.J., Schubert,V., Zhai,J., Pellegrini,M. and Jacobsen,S.E. (2014) Genome-wide Hi-C analyses in wild-type and mutants reveal high-resolution chromatin interactions in Arabidopsis. *Mol. Cell*, **55**, 694–707.

43. Grob,S., Schmid,M.W. and Grossniklaus,U. (2014) Hi-C Analysis in Arabidopsis Identifies the KNOT, a Structure with Similarities to the flamenco Locus of Drosophila. *Molecular Cell*, **55**, 678–693.

44. Wang,C., Liu,C., Roqueiro,D., Grimm,D., Schwab,R., Becker,C., Lanz,C. and Weigel,D. (2015) Genome-wide analysis of local chromatin packing inArabidopsis thaliana. *Genome Research*, **25**, 246–256.

45. Liu,C., Wang,C., Wang,G., Becker,C., Zaidem,M. and Weigel,D. (2016) Genome-wide analysis of chromatin packing in Arabidopsis thaliana at single-gene resolution. *Genome Research*, **26**, 1057–1068.

46. Fransz,P., De Jong,J.H., Lysak,M., Castiglione,M.R. and Schubert,I. (2002) Interphase chromosomes in Arabidopsis are organized as well defined chromocenters from which euchromatin loops emanate. *Proc. Natl. Acad. Sci. U. S. A.*, **99**, 14584–14589.

47. Schubert,I. and Shaw,P. (2011) Organization and dynamics of plant interphase chromosomes. *Trends in Plant Science*, **16**, 273–281.

48. Armstrong,S.J., Franklin,F.C. and Jones,G.H. (2001) Nucleolus-associated telomere clustering and pairing precede meiotic chromosome synapsis in Arabidopsis thaliana. *J. Cell Sci.*, **114**, 4207–4217.

49. Berr,A. and Schubert,I. (2007) Interphase Chromosome Arrangement in Arabidopsis thaliana Is Similar in Differentiated and Meristematic Tissues and Shows a Transient Mirror Symmetry After Nuclear Division. *Genetics*, **176**, 853–863.

50. Pontvianne,F., Carpentier,M.-C., Durut,N., Pavlištová,V., Jaške,K., Schořová,Š., Parrinello,H., Rohmer,M., Pikaard,C.S., Fojtová,M., *et al.* (2016) Identification of Nucleolus-Associated Chromatin Domains Reveals a Role for the Nucleolus in 3D Organization of the A. thaliana Genome. *Cell Rep.*, **16**, 1574–1587.

51. Sequeira-Mendes,J. and Gutierrez,C. (2016) Genome architecture: from linear organisation of chromatin to the 3D assembly in the nucleus. *Chromosoma*, **125**, 455–469.

52. Fang,Y. and Spector,D.L. (2005) Centromere Positioning and Dynamics in LivingArabidopsisPlants. *Molecular Biology of the Cell*, **16**, 5710–5718.

53. Bi,X., Cheng,Y.-J., Hu,B., Ma,X., Wu,R., Wang,J.-W. and Liu,C. (2017) Nonrandom domain organization of the genome at the nuclear periphery.

Genome Res., **27**, 1162–1173.

54. Zhou,S., Jiang,W., Zhao,Y. and Zhou,D.-X. (2019) Single-cell three-dimensional genome structures of rice gametes and unicellular zygotes. *Nat Plants*, **5**, 795–800.

55. Liu,C., Cheng,Y.-J., Wang,J.-W. and Weigel,D. (2017) Prominent topologically associated domains differentiate global chromatin packing in rice from Arabidopsis. *Nat Plants*, **3**, 742–748.

56. Yu,N., Nützmann,H.-W., MacDonald,J.T., Moore,B., Field,B., Berriri,S., Trick,M., Rosser,S.J., Kumar,S.V., Freemont,P.S., *et al.* (2016) Delineation of metabolic gene clusters in plant genomes by chromatin signatures. *Nucleic Acids Res.*, **44**, 2255–2265.

57. Nooijer,S. de, de Nooijer,S., Wellink,J., Mulder,B. and Bisseling,T. (2009) Non-specific interactions are sufficient to explain the position of heterochromatic chromocenters and nucleoli in interphase nuclei. *Nucleic Acids Research*, **37**, 3558–3568.

58. Roudier,F., Ahmed,I., Bérard,C., Sarazin,A., Mary-Huard,T., Cortijo,S., Bouyer,D., Caillieux,E., Duvernois-Berthet,E., Al-Shikhley,L., *et al.* (2011) Integrative epigenomic mapping defines four main chromatin states in Arabidopsis. *EMBO J.*, **30**, 1928–1938.

59. Sequeira-Mendes,J., Aragüez,I., Peiró,R., Mendez-Giraldez,R., Zhang,X., Jacobsen,S.E., Bastolla,U. and Gutierrez,C. (2014) The Functional Topography of the Arabidopsis Genome Is Organized in a Reduced Number of Linear Motifs of Chromatin States. *Plant Cell*, **26**, 2351–2366.

60. Simon,L., Voisin,M., Tatout,C. and Probst,A.V. (2015) Structure and Function of Centromeric and Pericentromeric Heterochromatin in Arabidopsis thaliana. *Front. Plant Sci.*, **6**, 1049.

61. Finch,J.T. and Klug,A. (1976) Solenoidal model for superstructure in chromatin.

Proc. Natl. Acad. Sci. U. S. A., **73**, 1897–1901.

62. Kremer,K. and Grest,G.S. (1990) Dynamics of entangled linear polymer melts: A molecular-dynamics simulation. *The Journal of Chemical Physics*, **92**, 5057–5086.

63. Di Stefano,M., Paulsen,J., Lien,T.G., Hovig,E. and Micheletti,C. (2016) Hi-C-constrained physical models of human chromosomes recover functionally-related properties of genome organization. *Sci. Rep.*, **6**, 35985.

64. Bystricky,K., Heun,P., Gehlen,L., Langowski,J. and Gasser,S.M. (2004) Long-range compaction and flexibility of interphase chromatin in budding yeast analyzed by high-resolution imaging techniques. *Proceedings of the National Academy of Sciences*, **101**, 16495–16500.

65. Grob,S., Schmid,M.W. and Grossniklaus,U. (2014) Hi-C analysis in Arabidopsis identifies the KNOT, a structure with similarities to the flamenco locus of Drosophila. *Mol. Cell*, **55**, 678–693.

66. Serra,F., Baù,D., Goodstadt,M., Castillo,D., Filion,G.J. and Marti-Renom,M.A. (2017) Automatic analysis and 3D-modelling of Hi-C data using TADbit reveals structural features of the fly chromatin colors. *PLoS Comput. Biol.*, **13**, e1005665.

67. Marco-Sola,S. and Ribeca,P. (2015) Efficient Alignment of Illumina-Like High-Throughput Sequencing Reads with the GEnomic Multi-tool (GEM) Mapper. *Curr. Protoc. Bioinformatics*, **50**, 11.13.1–20.

68. Vidal,E., le Dily,F., Quilez,J., Stadhouders,R., Cuartero,Y., Graf,T., Marti-Renom,M.A., Beato,M. and Filion,G.J. (2018) OneD: increasing reproducibility of Hi-C samples with abnormal karyotypes. *Nucleic Acids Res.*, **46**, e49.

69. Yan,K.-K., Yardimci,G.G., Yan,C., Noble,W.S. and Gerstein,M. (2017) HiC-spector: a matrix library for spectral and reproducibility analysis of Hi-C

contact maps. *Bioinformatics*, **33**, 2199–2201.

70. Fudenberg,G. and Imakaev,M. (2017) FISH-ing for captured contacts: towards reconciling FISH and 3C. *Nat. Methods*, **14**, 673–678.

71. Cattoni,D.I., Cardozo Gizzi,A.M., Georgieva,M., Di Stefano,M., Valeri,A., Chamousset,D., Houbron,C., Déjardin,S., Fiche,J.-B., González,I., *et al.* (2017) Single-cell absolute contact probability detection reveals chromosomes are organized by multiple low-frequency yet specific interactions. *Nat. Commun.*, **8**, 1753.

72. Dekker,J. (2008) Mapping in vivo chromatin interactions in yeast suggests an extended chromatin fiber with regional variation in compaction. *J. Biol. Chem.*, **283**, 34532–34540.

73. Strom,A.R., Emelyanov,A.V., Mir,M., Fyodorov,D.V., Darzacq,X. and Karpen,G.H. (2017) Phase separation drives heterochromatin domain formation. *Nature*, **547**, 241–245.

74. MacPherson,Q., Beltran,B. and Spakowitz,A.J. (2018) Bottom–up modeling of chromatin segregation due to epigenetic modifications. *Proceedings of the National Academy of Sciences*, **115**, 12739–12744.

75. Larson,A.G., Elnatan,D., Keenen,M.M., Trnka,M.J., Johnston,J.B., Burlingame,A.L., Agard,D.A., Redding,S. and Narlikar,G.J. (2017) Liquid droplet formation by HP1α suggests a role for phase separation in heterochromatin. *Nature*, **547**, 236–240.

76. Trussart,M., Serra,F., Baù,D., Junier,I., Serrano,L. and Marti-Renom,M.A. (2015) Assessing the limits of restraint-based 3D modeling of genomes and genomic domains. *Nucleic Acids Res.*, **43**, 3465–3477.

77. Serra,F., Di Stefano,M., Spill,Y.G., Cuartero,Y., Goodstadt,M., Baù,D. and Marti-Renom,M.A. (2015) Restraint-based three-dimensional modeling of genomes and genomic domains. *FEBS Lett.*, **589**, 2987–2995.

78. Dittmer,T.A., Stacey,N.J., Sugimoto-Shirasu,K. and Richards,E.J. (2007) LITTLE NUCLEI genes affecting nuclear morphology in Arabidopsis thaliana. *Plant Cell*, **19**, 2793–2803.

79. Tiang,C.-L., He,Y. and Pawlowski,W.P. (2012) Chromosome organization and dynamics during interphase, mitosis, and meiosis in plants. *Plant Physiol.*, **158**, 26–34.

80. Rosa,A., Di Stefano,M. and Micheletti,C. (2019) Topological Constraints in Eukaryotic Genomes and How They Can Be Exploited to Improve Spatial Models of Chromosomes. *Frontiers in Molecular Biosciences*, **6**.

81. Andrey,P., Kiêu,K., Kress,C., Lehmann,G., Tirichine,L., Liu,Z., Biot,E., Adenot,P.-G., Hue-Beauvais,C., Houba-Hérin,N., *et al.* (2010) Statistical analysis of 3D images detects regular spatial distributions of centromeres and chromocenters in animal and plant nuclei. *PLoS Comput. Biol.*, **6**, e1000853.

82. Wong,H., Marie-Nelly,H., Herbert,S., Carrivain,P., Blanc,H., Koszul,R., Fabre,E. and Zimmer,C. (2012) A predictive computational model of the dynamic 3D interphase yeast nucleus. *Curr. Biol.*, **22**, 1881–1890.

83. Kalhor,R., Tjong,H., Jayathilaka,N., Alber,F. and Chen,L. (2011) Genome architectures revealed by tethered chromosome conformation capture and population-based modeling. *Nat. Biotechnol.*, **30**, 90–98.

84. Di Stefano,M., Di Giovanni,F., Pozharskaia,V., Gomar-Alba,M., Baù,D., Carey,L.B., Marti-Renom,M.A. and Mendoza,M. (2020) Impact of Chromosome Fusions on 3D Genome Organization and Gene Expression in Budding Yeast. *Genetics*, 10.1534/genetics.119.302978.

85. Pawar,V., Poulet,A., Détourné,G., Tatout,C., Vanrobays,E., Evans,D.E. and Graumann,K. (2016) A novel family of plant nuclear envelope-associated proteins. *J. Exp. Bot.*, **67**, 5699–5710.

86. Hu,B., Wang,N., Bi,X., Karaaslan,E.S., Weber,A.-L., Zhu,W., Berendzen,K.W.

and Liu,C. (2019) Plant lamin-like proteins mediate chromatin tethering at the nuclear periphery. *Genome Biol.*, **20**, 87.

87. Kind,J., Pagie,L., Ortabozkoyun,H., Boyle,S., de Vries,S.S., Janssen,H., Amendola,M., Nolen,L.D., Bickmore,W.A. and van Steensel,B. (2013) Single-cell dynamics of genome-nuclear lamina interactions. *Cell*, **153**, 178–192.

88. Kind,J., Pagie,L., de Vries,S.S., Nahidiazar,L., Dey,S.S., Bienko,M., Zhan,Y., Lajoie,B., de Graaf,C.A., Amendola,M., *et al.* (2015) Genome-wide Maps of Nuclear Lamina Interactions in Single Human Cells. *Cell*, **163**, 134–147.

89. Paulsen,J., Liyakat Ali,T.M. and Collas,P. (2018) Computational 3D genome modeling using Chrom3D. *Nat. Protoc.*, **13**, 1137–1152.

90. Falk,M., Feodorova,Y., Naumova,N., Imakaev,M., Lajoie,B.R., Leonhardt,H., Joffe,B., Dekker,J., Fudenberg,G., Solovei,I., *et al.* Heterochromatin drives organization of conventional and inverted nuclei. 10.1101/244038.

91. Sati,S., Bonev,B., Szabo,Q., Jost,D., Bensadoun,P., Serra,F., Loubiere,V., Papadopoulos,G.L., Rivera-Mulia,J.-C., Fritsch,L., *et al.* (2020) 4D Genome Rewiring during Oncogene-Induced and Replicative Senescence. *Mol. Cell*, 10.1016/j.molcel.2020.03.007.

92. Tavares-Cadete,F., Norouzi,D., Dekker,B., Liu,Y. and Dekker,J. Multi-contact 3C data reveal that the human genome is largely unentangled. 10.1101/2020.03.03.975425.

93. Giorgetti,L. and Heard,E. (2016) Closing the loop: 3C versus DNA FISH. *Genome Biol.*, **17**, 215.

94. Rao,S.S.P., Huntley,M.H., Durand,N.C., Stamenova,E.K., Bochkov,I.D., Robinson,J.T., Sanborn,A.L., Machol,I., Omer,A.D., Lander,E.S., *et al.* (2015) A 3D Map of the Human Genome at Kilobase Resolution Reveals Principles of Chromatin Looping. *Cell*, **162**, 687–688.

95. Tjong,H., Li,W., Kalhor,R., Dai,C., Hao,S., Gong,K., Zhou,Y., Li,H., Zhou,X.J., Le

Gros,M.A., *et al.* (2016) Population-based 3D genome structure analysis reveals driving forces in spatial genome organization. *Proc. Natl. Acad. Sci. U. S. A.*, **113**, E1663–72.

96. McStay,B. and Grummt,I. (2008) The epigenetics of rRNA genes: from molecular to chromosome biology. *Annu. Rev. Cell Dev. Biol.*, **24**, 131–157.

97. Grummt,I. and Längst,G. (2013) Epigenetic control of RNA polymerase I transcription in mammalian cells. *Biochim. Biophys. Acta*, **1829**, 393–404.

98. Morf,J., Wingett,S.W., Farabella,I., Cairns,J., Furlan-Magaril,M., Jiménez-García,L.F., Liu,X., Craig,F.F., Walker,S., Segonds-Pichon,A., *et al.* (2019) RNA proximity sequencing reveals the spatial organization of the transcriptome in the nucleus. *Nat. Biotechnol.*, **37**, 793–802.

99. Sabari,B.R., Dall'Agnese,A., Boija,A., Klein,I.A., Coffey,E.L., Shrinivas,K., Abraham,B.J., Hannett,N.M., Zamudio,A.V., Manteiga,J.C., *et al.* (2018) Coactivator condensation at super-enhancers links phase separation and gene control. *Science*, **361**.

100. Lu,H., Yu,D., Hansen,A.S., Ganguly,S., Liu,R., Heckert,A., Darzacq,X. and Zhou,Q. (2018) Phase-separation mechanism for C-terminal hyperphosphorylation of RNA polymerase II. *Nature*, **558**, 318–323.

101. Pierro,M.D., Di Pierro,M., Zhang,B., Aiden,E.L., Wolynes,P.G. and Onuchic,J.N. A Transferable Model For Chromosome Architecture. 10.1101/048439.

102. Nuebler,J., Fudenberg,G., Imakaev,M., Abdennur,N. and Mirny,L.A. (2018) Chromatin organization by an interplay of loop extrusion and compartmental segregation. *Proc. Natl. Acad. Sci. U. S. A.*, **115**, E6697–E6706.

103. Pereira,M.C.F., Brackley,C.A., Michieletto,D., Annunziatella,C., Bianco,S., Chiariello,A.M., Nicodemi,M. and Marenduzzo,D. Complementary chromosome folding by transcription factors and cohesin. 10.1101/305359.

104. Ho,J.W.K., Jung,Y.L., Liu,T., Alver,B.H., Lee,S., Ikegami,K., Sohn,K.-A.,

Minoda,A., Tolstorukov,M.Y., Appert,A., *et al.* (2014) Comparative analysis of metazoan chromatin organization. *Nature*, **512**, 449–452.

105. Haddad,N., Vaillant,C. and Jost,D. (2017) IC-Finder: inferring robustly the hierarchical organization of chromatin folding. *Nucleic Acids Res.*, **45**, e81.

106. Chuang,C.-H., Carpenter,A.E., Fuchsova,B., Johnson,T., de Lanerolle,P. and Belmont,A.S. (2006) Long-range directional movement of an interphase chromosome site. *Curr. Biol.*, **16**, 825–831.

107. Mehta,I.S., Amira,M., Harvey,A.J. and Bridger,J.M. (2010) Rapid chromosome territory relocation by nuclear motor activity in response to serum removal in primary human fibroblasts. *Genome Biol.*, **11**, R5.

108. Fili,N. and Toseland,C.P. (2019) Unconventional Myosins: How Regulation Meets Function. *Int. J. Mol. Sci.*, **21**.

109. O'Toole,E.T., Winey,M. and Richard McIntosh,J. (1999) High-Voltage Electron Tomography of Spindle Pole Bodies and Early Mitotic Spindles in the Yeast Saccharomyces cerevisiae. *Molecular Biology of the Cell*, **10**, 2017–2031.

110. Hintze,J.L. and Nelson,R.D. (1998) Violin Plots: A Box Plot-Density Trace Synergism. *The American Statistician*, **52**, 181.

111. Humphrey,W., Dalke,A. and Schulten,K. (1996) VMD: Visual molecular dynamics. *Journal of Molecular Graphics*, **14**, 33–38.